Results in Engineering 28 (2025) 107659

Contents lists available at ScienceDirect

Results in Engineering

journal homepage: www.sciencedirect.com/journal/results-in-engineering

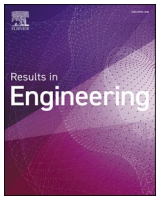

Research paper

Computational evaluation of the impact of low-modulus beta-titanium alloys on stress shielding of tibial trays in cementless total knee replacements

Jan-Oliver Sass *, Jonas Wenschuh, Florence Kosche, Rainer Bader, Maeruan Kebbach

Research Laboratory for Biomechanics and Implant Technology, Department of Orthopedics, Rostock University Medical Center, Rostock, Germany

ARTICLE INFO

Keywords:
Total knee replacement
Musculoskeletal multibody simulation
Finite element simulation
Gaussian process regression
Implant material
Beta-titanium

ABSTRACT

The implant's material properties influence aseptic loosening in total knee replacement. This study aimed to computationally analyze the biomechanical performance of the tibial tray, considering a wide range of titanium-based implant materials featuring open porous surfaces. A combined musculoskeletal multibody and finite element simulation of a total knee replacement during a squat motion trained surrogate models to predict periprosthetic bone strain energy and tibial tray stress. The analysis considered variations in the Young's modulus of the tibial tray (YM_T: 40 – 120 GPa), Young's modulus of the open porous surface (YM_S: 0 – 10 GPa), and surface thickness (S_T: 0 – 2 mm). A Pareto front analysis revealed optimal biomechanical behavior for material and design combinations of $YM_T = 40$ GPa, $YM_S = 2$ GPa, and $S_T = 2$ mm. This configuration resulted in a 48.5% reduction in the volume of periprosthetic bone exposed to critical loading levels linked to disuse-related osteolyses. Maximum von Mises stresses, reaching 116.7 MPa, were localized at the transition between solid and open porous materials and remained below the reported fatigue limits for beta-titanium alloys. These preliminary findings establish foundational material property ranges for beta-titanium alloys, providing a basis for future research on optimizing alloy compositions and implant designs to enhance mechanical performance and long-term fatigue resistance in cementless tibial trays.

1. Introduction

Total knee replacement is an effective procedure for replacing the degenerated knee joint in end-stage osteoarthritis and restoring functionality with good long-term clinical outcomes [1]. A major cause of failure is aseptic loosening, accounting for 16.3 − 39.5 % of all failures based on the registry data from 11 countries [2]. Aseptic implant loosening is partly traced back to material-related factors, i.e., osteolysis due to wear and corrosion [3–6] and periprosthetic bone disuse atrophy due to stress shielding phenomena [7–9]. These effects result in a reduction in periprosthetic bone density [10,11]. Stress shielding is caused by an altered loading condition of the bone after implantation of a significantly stiffer implant material [8,10,12] and is primarily influenced by the intrinsic mechanical properties [9]. In addition to the loosening of the implant components, these effects also contribute to the development of proximal tibial bone defects that require specific augmentation during revision surgery [11,13,14]. These defects can alter the loading condition of the tibial tray, comparable to unilateral fatigue loading as defined by standards [15,16], and potentially lead to fatigue fracture [17,18].

The most commonly used material for the tibial tray is Ti-6Al-4V, which has a Young's modulus of approximately 110 GPa [19]. In contrast, human bone typically has a Young's modulus of ≤ 20 GPa [20,21], highlighting the mechanical mismatch. To address this limitation, studies have explored less stiff materials such as polyethylene (all-polyethylene tibial components) [9,22], and poly-ether-ether-ketone (PEEK) [23]. Moreover, low-modulus cubic room-centered beta-titanium alloys have been experimentally characterized [24–29], but they have not been comprehensively evaluated for application in cementless total knee replacements. Biomedical beta-titanium alloys are noted for their alloying components such as niobium, tantalum, and zirconium, which exhibit high biocompatibility [30] and stabilize the β-phase. Several studies have shown lower stiffness [24–28], improved biocompatibility [24], and high corrosion resistance [29], demonstrating

* Corresponding author at: Research Laboratory for Biomechanics and Implant Technology, Department of Orthopedics, Rostock University Medical Center, Doberaner Straße 142, D-18057 Rostock.

E-mail address: jan-oliver.sass@med.uni-rostock.de (J.-O. Sass).

https://doi.org/10.1016/j.rineng.2025.107659
Received 19 May 2025; Received in revised form 30 September 2025; Accepted 8 October 2025
Available online 10 October 2025

potential to enhance bone-implant interaction, particularly in the long term.

In addition to the intrinsic material properties, additive manufacturing (e.g., laser beam powder bed fusion) of titanium alloys offers opportunities for topology optimization [31,32] or physical functionalization of the implant surfaces in contact with human bone [12,24,33–36]. Open porous structures can exhibit a stiffness in the range of human trabecular or cortical bone [20,21,24,37–40], thus, favoring lower stress shielding. Moreover, these structures promote improved osseointegration due to higher primary stability (small micro-motions) and also more stable secondary stability due to increased bone growth kinetics and complete penetration of bone throughout the open porous structure [35].

Nevertheless, the use of beta-titanium alloys in orthopedic implants poses challenges. Depending on the chemical composition, microstructure, and surface properties, the strength [19,41] and fatigue endurance [28,37,42–46] of beta-titanium alloys may be reduced compared to Ti-6Al-4V. More precisely, fatigue strengths of 430 – 624 MPa [37,43] have been reported for Ti-6Al-4V, while Günther et al. [42] reported 275 – 300 MPa for Ti-42Nb (produced by laser beam powder bed fusion). Therefore, the applicability of beta-titanium alloys for specific implants needs to be demonstrated. Although tibial tray fatigue fractures rarely occur with the currently used Ti-6Al-4V [17,18], their likelihood must not be increased with alternative implant materials. However, there is a lack of pre-clinical evaluations conducted under relevant biomechanical conditions, which are essential to assess the performance of implant designs.

In this context. the finite element (FE) method has been used to analyze the bone-implant interaction of tibial trays of total knee replacements made of different materials [9,22,23,47–49] or bone conditions, i.e., tibial bone defects [13,14] or osteoporotic bone conditions [23]. However, these studies focused on static loading cases rather than active movements of the patient through a high range of motion, such as squatting, which provides a broader insight into the biomechanical performance [10,50,51]. In addition, the interdependencies of the tibial tray material and design, i.e., different titanium-based alloys and open-porous surface structures, have not been investigated so far under varying bone conditions.

Therefore, this computational study aimed to systematically investigate the influence of the implant material and the characteristics of the open porous surface of the tibial tray on stress shielding in the periprosthetic bone and stress distribution in the tibial tray during a two-legged squat motion, considering two different tibial bone conditions (intact vs. medial defect). To accomplish this goal, we combined individualized musculoskeletal multibody simulation (MMBS) with an FE simulation that varied the Young's modulus of the tibial tray (dense part and open-porous surface) and the thickness of the open-porous surface. These models were used to train Gaussian Process Regression (GPR) models as surrogates to expand the data set and, finally, perform a Pareto front analysis to determine the best-performing parameter combinations in terms of bone strain energy in normal bone conditions and stresses in the tibial tray under severe loading conditions caused by a medial tibia bone defect.

2. Materials and methods

2.1. Components and general assumptions of the finite-element model

The FE model, consisting of the tibial bone and a total knee replacement (tibial tray, tibial insert and femoral component), was developed in Abaqus 2022 (Dassault Systèmes, Providence, RI, USA) and followed the quasi-static implicit analysis scheme. A cruciate-retaining fixed-bearing total knee replacement (Columbus®, Aesculap AG, Tuttlingen, Germany) was used. The tibia (male, 75 years old) was reconstructed from CT images using Mimics 25.0 (Materialize NV, Leuven, Belgium). According to Kluess et al. [52], Geomagic Studio 2013 (Geomagic Inc., Morrisville, USA) was used to generate the 3D volume part of the tibial bone. The proximal tibia was either modeled completely intact or with a virtually generated artificial medial bone defect 10 mm in height, based on previous studies [11,14] (see Fig. 1). The defect model was used to study implant loading under severe conditions, which are comparable to those defined in standards for experimental testing of tibial tray fatigue endurance [16].

The tibial tray was virtually implanted according to the manufacturer's guidelines in Creo Parametric (v10.0.0.0, PTC Inc., Boston, MA, USA), and based on the positioning of the implant components in the MMBS.

2.2. Boundary and loading conditions

The boundary and loading conditions of the FE model were calculated using an MMBS during a squat movement using the same total knee replacement. The computational approach to transfer the calculated knee joint dynamics (translations, rotations, axial force) from the MMBS to the FE model has been previously described in detail [53]. Briefly, the MMBS was based on the 4th Grand Knee Challenge dataset [54], built in SIMPACK (v9.7 Dassault Systèmes, Providence, RI, USA), and all model characteristics, i.e. geometries, motion capture data, soft tissue properties, and contact properties were described in previous studies [55–57]. The MMBS model calculated the tibiofemoral joint dynamics during a two-leg squat to ~90° of knee flexion. The outputs of the MMBS model were transferred to a fixed local coordinate system (K_{TF}), which is also defined in the FE model (see Fig. 1). Concretely, the joint dynamics were used as forces (in N), translations (in mm), or rotations (in radians) and applied to a reference point (origin of the local coordinate system K_{TF}) that was kinematically coupled to the inner surface of the femoral component. The distal end of the tibial bone was constrained to zero degrees of freedom during the entire squat motion. The movement was performed within 1 s, and FE model outputs were derived every 0.05 s for post-processing.

2.3. Material properties

All materials were assumed to have isotropic, linear elastic mechanical properties, and the specifications are summarized in Table 1. Except for the tibial bone, the materials were modeled homogenous. The heterogeneous bone properties were assigned based on the CT data. A self-written MATLAB script (2024a, The Mathworks Inc., Natick, MA, USA) was used to assign a nodal temperature to each node of the finite element model based on the Hounsfield Units (HU) of the corresponding voxel. A partial volume correction of surface nodes was performed by assigning HU values of the nearest internal node, if the HU at the internal node is higher than that of the surface node. In this manner, a virtual temperature-dependent Young's modulus was defined to account for the heterogeneity of the bone [58]. The modulus-density relationships of Rho et al. [20] were used for the cortical and trabecular bone of the tibia in the superior-inferior direction. Since no phantom was present in the CT scan, the correlation between HU value and apparent density was determined by defining the maximum HU value of the cortical bone with an apparent density ρ of 1.8 g/cm^3 and assigning an apparent density ρ of 0.0012 g/cm^3 to the HU value of air with −1000 [59,60]. The linear correlation function is $\rho = 376.5 + 0.4 \times HU$ [kg/m^3] with ρ: apparent density and HU: Hounsfield Unit.

A representative cut view of the tibial bone with the heterogeneous

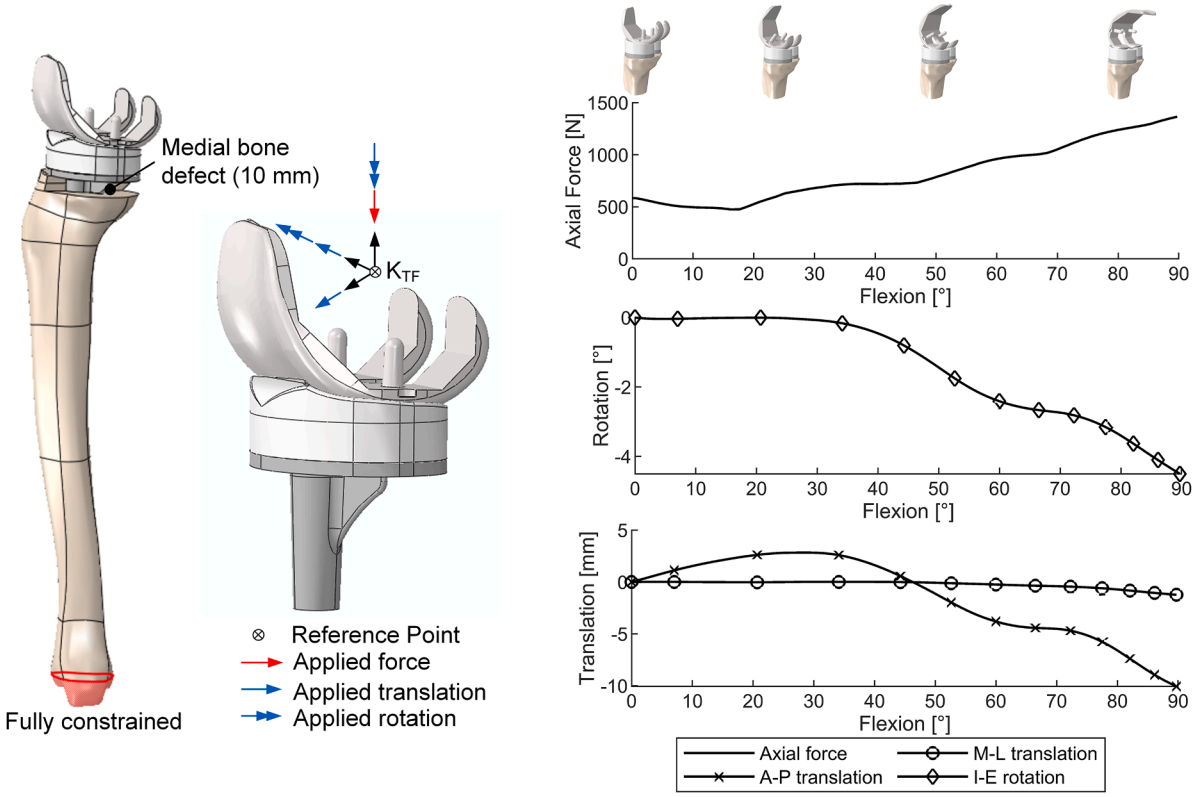

Fig. 1. Illustration of the finite element model components from top to bottom: femoral component, tibial insert, tibial tray, tibial bone (intact or medial defect, the latter shown as an example), the local coordinate system $K_{TF,}$ and the acting axial force, translations (anterior-posterior (A-P), medio-lateral (M-L), and rotations (flexion, internal-external (I-E)) that were extracted from the musculoskeletal multibody simulation during the squat movement using the same total knee replacement.

Table 1
Overview of the model components and the assumed mechanical properties.

Component	Material	Young's modulus	Poisson`s ratio	
Tibial bone	Tissue	Cortical: $-3.842 + 0.013\rho$ [GPa] Trabecular: $-326 + 5.54\rho$ [MPa]	0.3	[20]
Femoral component	CoCrMo alloy	Rigid body	-	[61]
Tibial insert	UHMW-PE	0.313 GPa	0.46	[62]
Tibial tray	Solid material[#]	40 – 120 in 20 GPa increments	0.33	
	Porous material[#]	2 – 10 in 2 GPa increments	0.33	

[#] Part of the sensitivity analysis

material properties based on the HU values is shown in Fig. A1 in the Appendix.

Following the objectives of this study, the titanium-based materials analyzed for the tibial tray covered a range of 40 to 120 GPa and, therefore, resembled low-modulus beta-titanium alloys [24–28] up to Ti-6Al-4V [19,41]. Furthermore, the open porous surface was modeled with a stiffness ranging from 2 to 10 GPa [24,33,40] and a thickness of 0 to 2 mm. The material and design parameters are further denoted as YM_T (Young's modulus of the tibial tray), YM_S (Young's modulus of the open porous surface), and S_T (thickness of the open porous surface). The thickness of the surface layer was not modeled geometrically. Instead, different Young's moduli were assigned to specific nodes that lie within the open porous surface layer and those within the dense tibial tray (see Fig. 2). The method followed the approach described by Roffman et al. [63], where Young's moduli are assigned to nodes based on their distance from a given surface. The node-wise mapping was done in MATLAB and implemented in Abaqus by a virtual temperature-dependent Young's modulus. Nodes that were within the surface layer were assigned a temperature of 0 and, equally, the specific Young's modulus of the open porous surface, and the remaining nodes were assigned a temperature of 1 and, equally, the specific Young's modulus of the dense tibial tray material. Fig. 2 shows different model variants with S_T 1 mm, and 2 mm. This approach had the advantages that no stress singularities occurred at the transition from dense to open porous material, the mesh configuration was similar for all models, and the time for model building in the sensitivity analysis was reduced because only the temperature

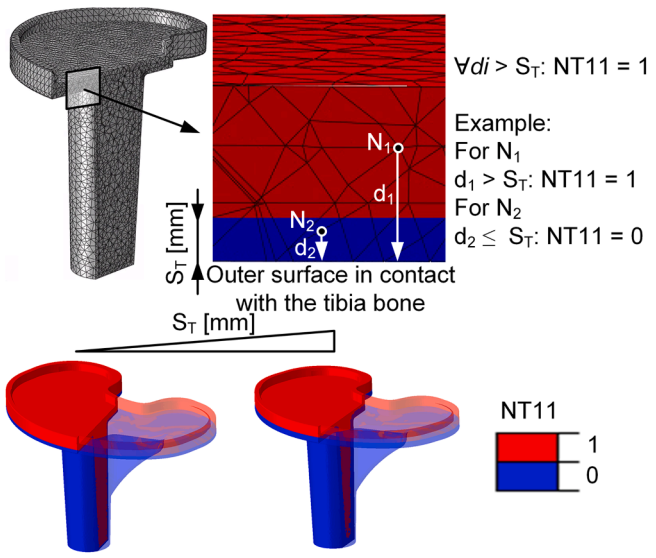

Fig. 2. Virtually assigned node temperature field of the tibial tray to account for different open porous surface thicknesses (S_T [mm]) ranging from 0 to 2 mm in 0.5 mm increments. For all nodes (N_i) that have a higher distance (d_i) to the outer surface that is in bone contact, the nodal temperature (Abaqus field output NT11) is 1, and all nodes with a distance smaller than or equal to the open porous surface thickness have a nodal temperature is 0. Different open porous surface thicknesses of the tibia tray (one half transparent to highlight the cross-section) are shown in the bottom figure, where blue represents the open porous surface and red the dense tibial tray material.

field had to be changed.

2.4. Contact properties

The contact between the bone and the tibial tray was assumed to be fully osseointegrated (tie-constrained). Furthermore, the contact between the tibial tray and the tibial insert was also constrained to zero degrees of freedom. A frictional contact with a coefficient of friction of 0.04 was defined for the articulating surfaces of the tibiofemoral joint, i.e., between the femoral component and tibial insert [53].

2.5. Model outputs

Two relevant model outputs were analyzed to evaluate the biomechanical performance. In the intact tibial bone models, the strain energy in the bone region of interest (ROI), defined at the proximal part in a 5 mm thick region of interest (ROI) [8,64], was analyzed. Furthermore, in the tibial bone defect model, the von Mises stresses within the tibial tray were analyzed.

2.6. Meshing

All model components were discretized with quadratic tetrahedral elements (C3D10), and a convergence study was performed on the defined model outputs. The convergence criteria were set to a change of the analyzed model outputs of less than 5 % to the next finer mesh. The elaborated element edge length of the bone ROI was 2.4 mm. The tibial tray was meshed with an element edge length of 1.5 mm, and a local mesh refinement (0.5 mm) was applied in the area of highest stresses in the medial part. The femoral component and the tibial insert were meshed with a mean element edge length of 5 mm and 4 mm, respectively.

2.7. Statistical analysis

To perform a comprehensive analysis of relevant model outputs in dependence on the implant material and design, computationally efficient surrogate models (Gaussian Process Regression, GPR [65]) were trained using MATLAB. Comparable approaches have been used previously in the field of orthopedic [66], dental [67,68], and cardiovascular implants [69] to efficiently analyze large parameter sets. The training set included 40 MMBS-FE models with random variations, derived by Latin Hypercube Sampling of the material and design parameters (Appendix, Table A1). We applied a hyperparameter optimization (Bayesian optimization), a leave-one-out cross-validation, and calculated the RMSE for each cross-validated GPR. Furthermore, the GPR models were used to evaluate all possible material and design combinations within the defined parameter space of YM_T, YM_S, and S_T ($n = 105$), where we assumed that if the surface thickness is zero, then the Young's modulus of the surface equals zero too.

Based on this dataset, the Pearson correlation coefficients of the model outputs and design parameters were calculated and further a multi-objective Pareto front analysis was conducted to maximize the strain energy in the bone ROI and minimize the stress in the tibial tray using MATLAB. For each time step of the squat motion, the Pareto optimal material and design combinations were defined. A material and design combination is Pareto optimal if no other feasible combination improves at least one of the objectives without worsening the other.

2.8. Comparison of the Pareto-optimal design to a Ti-6Al-4V reference

Based on the identified Pareto-optimal parameter combination during the squat motion, the strain energy within the periprosthetic bone and the maximum stress in the tibial tray were calculated using the MMBS-FE model. For comparison, a reference model was defined featuring a tibial tray composed of Ti-6Al-4V (Young's modulus: 110 GPa) without an open porous surface.

To facilitate a detailed evaluation, the strain in the periprosthetic bone ROI was assessed with respect to mechanostat theory of Frost [70], categorizing regions into disuse (<50 μstrain), physiological loading (50–3,000 μstrain), overuse (3,000–25,000 μstrain), and overload (>25,000 μstrain). Furthermore, the maximum von Mises stresses and the difference between the maximum and minimum von Mises stress within a loading cycle, i.e. the von Mises stress range [71], were evaluated in both the porous surface and solid tray to enable a comparative assessment against the fatigue limit of beta-titanium alloys and comparable FE studies.

3. Results

The MMBS-FE model was used to calculate 40 sampled models with varying material and design parameters (specifications are shown in Table A1 in the appendix). Representative results of a model with a Young`s modulus of the tibial tray of 100 GPa without an open porous surface are shown in Fig. 3. The strain energy and maximum stress increased for higher flexion angles. The maximum stress was observed on the medial side of the tibial tray and at the transition of the baseplate to the stem. During the squat motion and the anterior movement of the femoral component, the maximum stress also translated anterior.

Table 2 shows the descriptive statistics (mean, standard deviation, minimum, maximum) of the strain energy in the periprosthetic bone and the maximum von Mises stress in the tibial tray during the squat motion across the 40 training models.

The Pearson correlation coefficients of the strain energy in the bone ROI and the stress in the tibial tray to the material and design

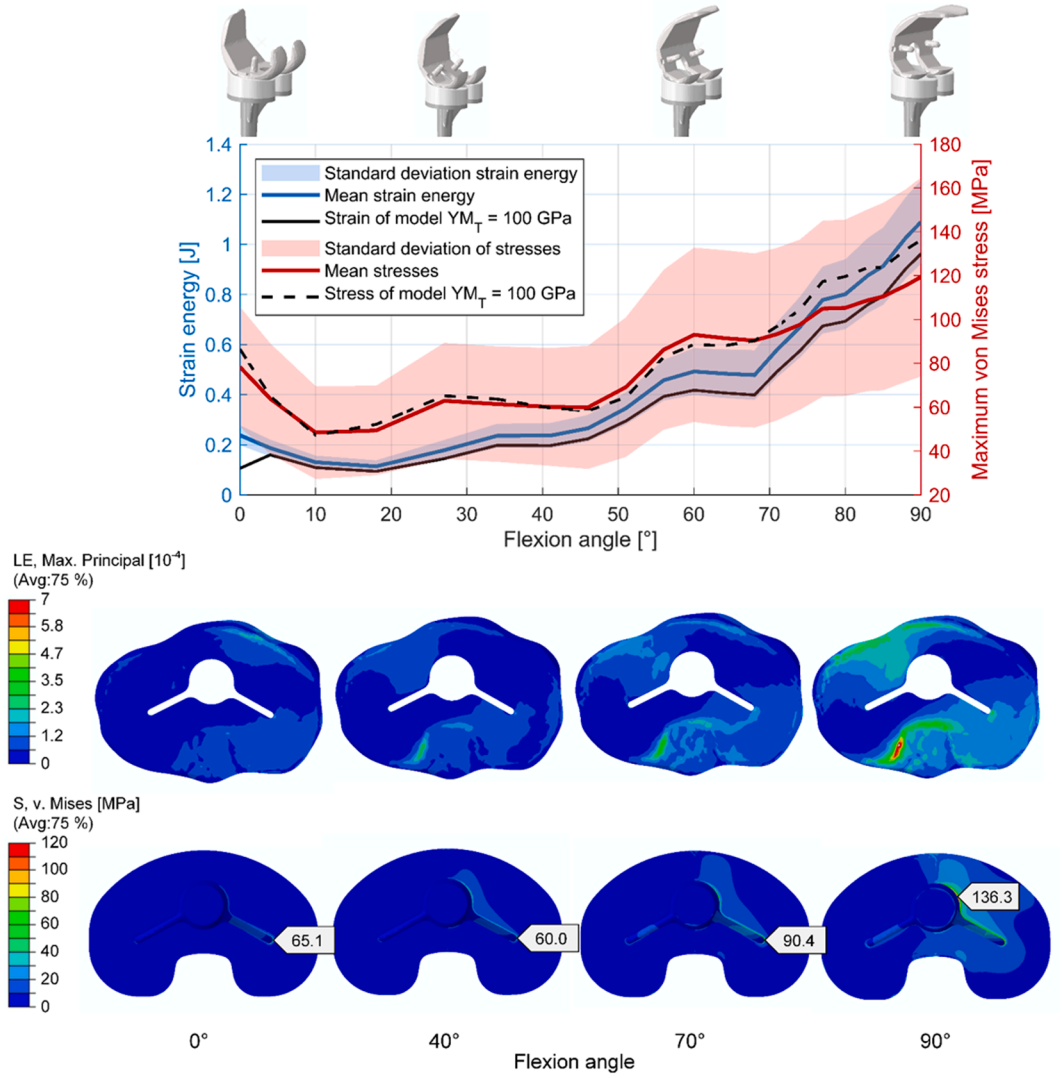

Fig. 3. Overview of the strain energy in the periprosthetic bone and the maximum von Mises stress during the squat motion, shown as mean and standard deviation of the training models as well as for a representative model with a Young`s modulus of 100 GPa of the tibial tray (YM_T) and without an open porous surface.

parameters are shown in Fig. 4 as a function of time within the squat motion.

The correlation analysis showed that the strain energy is negatively correlated with the Young's modulus of the tibial tray (averaged over the entire squat motion: $r = -0.54$), not linearly related to the Young's modulus of the open porous surface (averaged over the entire squat motion: $r = 0.04$), and positively correlated with the thickness of the open porous surface (averaged over the entire squat motion: $r = 0.89$). Correlation analysis of the stress in the tibial tray showed a slight correlation to the Young's modulus of the tibial tray (averaged over the entire squat motion: $r = 0.24$) and the thickness of the open porous surface (averaged over the entire squat motion: $r = 0.29$) as well as a negative correlation with the Young's modulus of the open porous surface (averaged over the entire squat motion: $r = -0.52$).

The leave-one-out cross-validation of the trained surrogate models yielded an average RMSE over the squat motion of 0.02 ± 0.01 J for strain energy and 5.4 ± 2.6 MPa for maximum stress. The RMSE over the squat motion is shown in Fig. A2 in the appendix. These surrogate models were subsequently used to predict the relevant model outputs across the entire parameter space. All optimal parameter combinations consistently featured a tibial tray with a Young's modulus of 40 GPa and an open porous surface thickness of 2 mm, and this trend was observed across all time steps. The identified Pareto-optimal parameter combinations are summarized in Table 3.

To further investigate the identified Pareto-optimal configurations, MMBS-FE models were employed to analyze two representative designs: YMT = 40 GPa, $YM_S = 2$ GPa, $S_T = 2$ mm (hereafter referred to as 40-2-2), and $YM_T = 40$ GPa, $YM_S = 10$ GPa, $S_T = 2$ mm (hereafter 40-10-2). These were compared against a reference model composed entirely of Ti-6Al-4V without an open porous surface.

The von Mises stresses observed, both Pareto-optimal designs resulted in a notable increase in strain energy density within the bone ROI. According to the mechanostat theory of bone remodeling, this mechanical stimulus corresponds to a reduction in disuse-related bone volume. Specifically, within the 5 mm thick proximal tibia ROI at 90° knee flexion, the volume of predicted disused bone decreased by 48.5% in model 40-2-2 and 40.0% in model 40-10-2 relative to the Ti-6Al-4V reference. Fig. 5B shows qualitatively the strain in the periprosthetic bone in relation to the mechanostat theory [70].

In general, von Mises stress within the tibial tray increased at higher

Table 2
Descriptive statistics (mean, standard deviation (SD), minimum, maximum) of the strain energy in J in the periprosthetic bone and the maximum von Mises stress in MPa in the tibial tray during the squat motion across the 40 training models.

Flexion angle [°]	Strain energy in the periprosthetic bone				Maximum von Mises stress in the tibial tray			
	Mean	SD	Min	Max	Mean	SD	Min	Max
0	0.24	0.04	0.17	0.32	78.3	27.5	30.2	165.6
4	0.19	0.03	0.13	0.26	63.9	25.2	24.4	147.7
10	0.13	0.03	0.09	0.19	48.4	21.2	20.6	119.1
18	0.11	0.02	0.07	0.16	49.4	20.4	20.1	117.0
27	0.18	0.04	0.11	0.26	62.9	26.5	26.5	149.9
34	0.24	0.05	0.16	0.33	61.4	26.3	27.1	147.8
41	0.24	0.05	0.15	0.34	60.1	26.9	27.3	148.9
46	0.27	0.05	0.18	0.38	60.0	28.1	27.8	152.0
51	0.35	0.06	0.24	0.48	69.2	31.8	31.4	174.2
56	0.46	0.08	0.32	0.63	86.2	36.4	36.3	207.0
60	0.49	0.09	0.33	0.69	93.0	39.7	39.4	224.8
64	0.48	0.10	0.32	0.69	91.5	40.1	40.0	223.8
68	0.48	0.10	0.31	0.68	90.4	39.7	40.1	220.4
71	0.58	0.11	0.39	0.80	93.4	39.3	41.2	221.8
74	0.67	0.12	0.46	0.91	97.7	38.8	42.6	224.8
77	0.78	0.13	0.54	1.04	105.0	40.1	44.4	235.4
80	0.80	0.14	0.56	1.08	105.3	40.2	45.0	235.0
83	0.88	0.15	0.61	1.17	108.8	41.5	46.2	242.6
85	0.91	0.15	0.64	1.21	110.5	42.7	47.6	248.8
88	1.03	0.16	0.73	1.34	115.5	43.9	49.1	256.5
90	1.09	0.17	0.78	1.41	119.4	45.4	50.6	265.4

knee flexion angles and corresponding axial loading, as shown in Fig. 6A. Among the Pareto-optimal parameter models, the stress at 90° knee flexion decreased by 27.3% in model 40-2-2 and by 60.8% in model 40-10-2, compared to the reference model (see Fig. 6B).

In the reference model, the maximum von Mises stress was localized at the sharp transition between the tibial baseplate and the stem, corresponding to an abrupt geometric discontinuity. In contrast, model 40-2-2 exhibited peak stress at the interface between the open porous surface and the solid region of the tibial tray, which can be seen in the cut view as shown in Fig. 6B. For model 40-10-2, the location of maximum stress was similar to that of the reference model but occurred within the open porous surface rather than the solid material. The von Mises stress ranges were 114.2 MPa (reference model), 111.0 MPa (model 40-2-2), and 54.0 MPa (model 40-10-2) with corresponding stress ratios R of 0.10 (reference model), 0.05 (model 40-2-2), and 0.14 (model 40-10-2), respectively.

4. Discussion

Aseptic implant loosening remains one of the leading causes of failure following total knee replacement [2]. A key contributing factor is the reduction in periprosthetic bone density, partly attributed to stress shielding [7–9]. To address this, prior studies have shown that implant materials with lower stiffness than conventional Ti-6Al-4V can reduce the risk of bone atrophy around the tibial tray [9,22,23,48]. Among these, biomedical beta-titanium alloys have demonstrated promising potential to enhance bone–implant interactions due to their favorable mechanical and biocompatible properties [24].

Specific clinical scenarios, such as unilateral tibial bone defects [11,13,14], lead to high demands on implant fatigue resistance [15,16], underscoring the need for a comprehensive evaluation of beta-titanium alloys under realistic conditions. In parallel, advancements in additive manufacturing enable both direct structural design modifications [31,32] and surface functionalization techniques [12,24,33–35], which are critical for improving osseointegration and promoting cementless primary fixation.

Despite these advances, there is still a lack of studies systematically evaluating beta-titanium alloys in cementless tibial trays, particularly under clinically relevant loading scenarios. While previous computational analyses have suggested that lower-stiffness materials may reduce periprosthetic stress shielding [9,22,23,48], they have generally considered narrow material parameter ranges and did not simulate high-risk loading conditions, such as those caused by unilateral bone defects. Furthermore, most models have only incorporated static loading cases [8,9,22,23,31,32,47,49,64], limiting their physiological relevance.

To address these limitations, the present study builds upon a previously validated MMBS-FE model [53], integrating a patient-specific squat motion up to 90° knee flexion. A comprehensive parameter space was defined to reflect the variability of beta-titanium alloys, with the Young's modulus of the tibial tray ranging from 40 to 120 GPa. For the open porous surface layer, the Young's modulus ranged from 2 to 10 GPa, and the thickness ranged from 0.5 to 2 mm. The objective of this study was to identify Pareto-optimal combinations of material and design parameters that concurrently minimize periprosthetic stress shielding and stress concentrations within the tibial tray.

Based on trained GPR surrogate models, Pareto front analysis revealed that the most promising configurations include a tibial tray Young's modulus of 40 GPa and a porous surface thickness of 2 mm. The optimal range for the porous surface modulus spanned from 2 to 10 GPa, offering flexibility in design while maintaining mechanical

Table 3
Identified Pareto optimal parameter combinations (YM_T: Young`s modulus of the solid tibial tray, $YM_S$: Young`s modulus of the open porous surface, ST: thickness of the open porous surface).

YM_T [GPa]	YM_S [GPa]	S_T [mm]
40	2	2
	4	
	6	
	8	
	10	

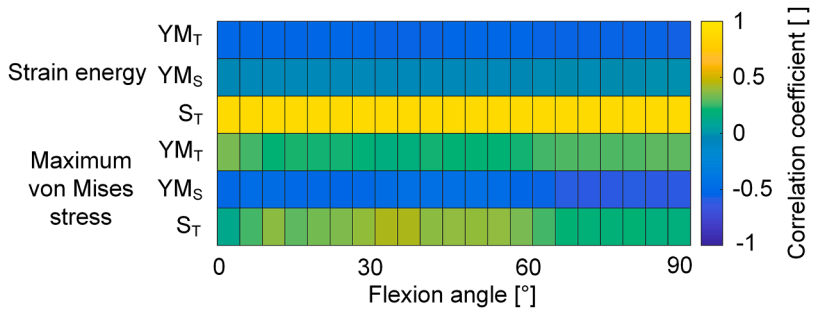

Fig. 4. Heatmap of the Pearson correlation coefficients between the strain energy in the proximal tibia bone ROI or stress in the tibial tray and the material and design parameters Young's modulus of the tibial tray (YM_T), Young's modulus of the open porous surface (YM_S) and thickness of the open porous surface (S_T) in dependence on the time during the squat motion.

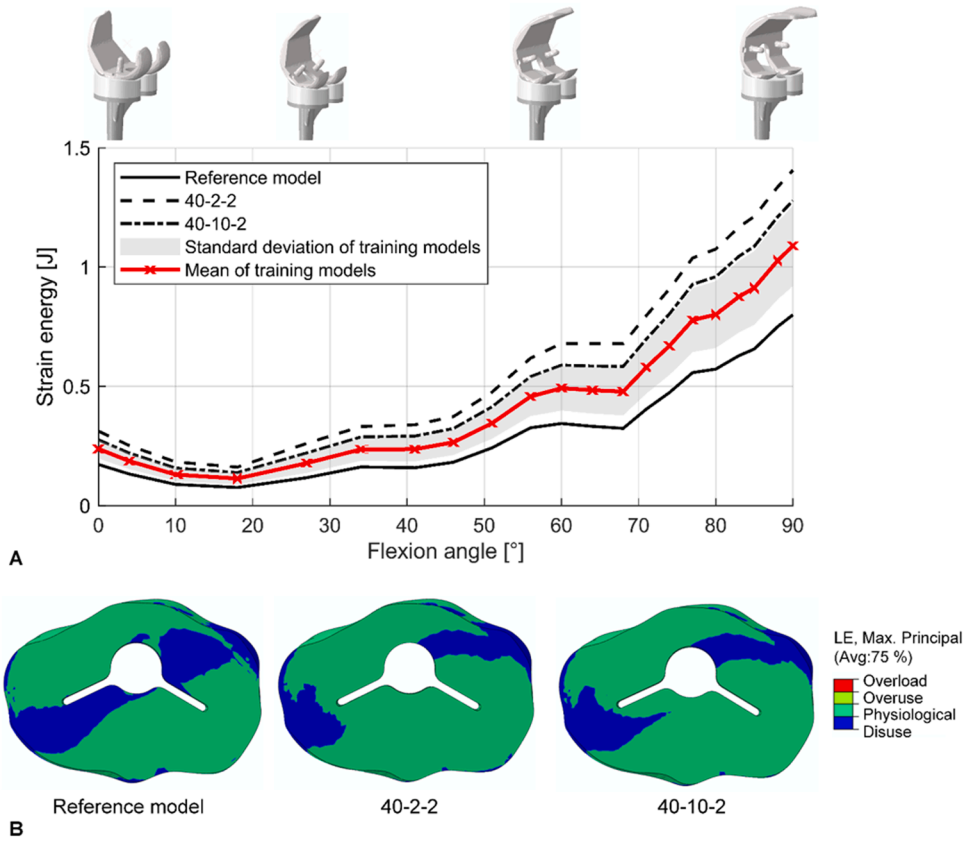

Fig. 5. Comparison of the reference model made of Ti-6Al-4V without an open porous surface and Pareto optimal parameter combinations of the Young`s modulus of the tibial tray (both 40 GPa), Young`s modulus of the open porous surface (2 or 10 GPa) and the thickness of the open porous surface (both 2 mm). A) Strain energy in the periprosthetic bone ROI in dependence on the flexion angle during the squat motion showing the mean and standard deviation of all training models as well as the Pareto optimal models and the reference model and B) Strain in the bone ROI in relation to the mechanostat theory [70] at 90° knee flexion.

performance.

The observed strain levels in the periprosthetic bone fell within a physiologically reasonable range [34,37]. However, direct comparison with other studies is limited due to variations in patient-specific bone properties and the applied motion sequence. Nevertheless, the general findings align with previous investigations into total knee replacement that explored the use of lower-stiffness implant materials [9,23,47,49,71] or modified implant designs [31,32] aimed at mitigating stress shielding in the periprosthetic bone. Correlation analysis within the defined parameter space showed that the thickness of the open porous surface is the most influential factor in reducing periprosthetic stress shielding. When comparing the identified Pareto-optimal combinations to the Ti-6Al-4V reference, and interpreting the results in the context of the mechanostat theory [70], the findings highlight a strong potential to decrease disuse-related osteolyses, i.e., a reduction of 48.5 % in the periprosthetic bone ROI in the case of the model 40-2-2. In addition, open porous beta-titanium structures have demonstrated an enhanced capacity to support osteogenic differentiation of human osteoblasts compared to Ti-6Al-4V [24], thereby further promoting osseointegration.

The locations of the observed stress concentrations in the tibial tray were consistent with findings from retrieval studies, which reported crack initiation at geometrical notches, i.e., transition from the baseplate to the stem, within the tibial tray [17,18]. The observed von Mises stress range (minimum to maximum within a loading cycle) in the reference model (144.2 MPa) was lower than those reported in a previous FE study (176 MPa) that simulated the unilateral loading condition prescribed by ASTM F2083 [72]. In the ASTM F2083 protocol, a cyclic unilateral load of up to 2 kN is applied, representing a standardized worst-case scenario. In contrast, the maximum axial force in the MMBS-FE models during a squat movement reached 1364 N, yet it was still only partially supported by the medial compartment. This indicates that while the applied squat motion reflects a physiologically demanding activity, it does not fully replicate the extreme loading conditions defined in ASTM F2083. Nevertheless, the variation in both the magnitude and location of peak stresses across the squat motion highlights the importance of simulating complete movement sequences. Changes in implant positioning throughout the motion alter load transfer patterns, resulting in shifting peak stress locations that would not be captured in static or simplified loading scenarios.

The correlation analysis indicated only a limited linear relationship between the input parameters and the peak stresses in the tibial tray. The strongest correlation was observed for the Young's modulus of the open porous surface ($r = -0.52$), suggesting a moderate inverse association. As illustrated in the comparison between the Ti-6Al-4V reference and the Pareto-optimal models, the location of peak stress is highly influenced by the mechanical characteristics of the open porous surface (see Fig. 6). A relatively low stiffness in this region (as in model 40-2-2) resulted in stress concentration at the transition zone between the solid tibial tray and the porous surface layer. Conversely, a stiffer open porous surface shifted the peak stresses into the porous surface structure.

In clinical application, the fatigue endurance of the tibial tray is a critical determinant of long-term implant success. Therefore, the observed stress levels must be evaluated relative to the fatigue limits of

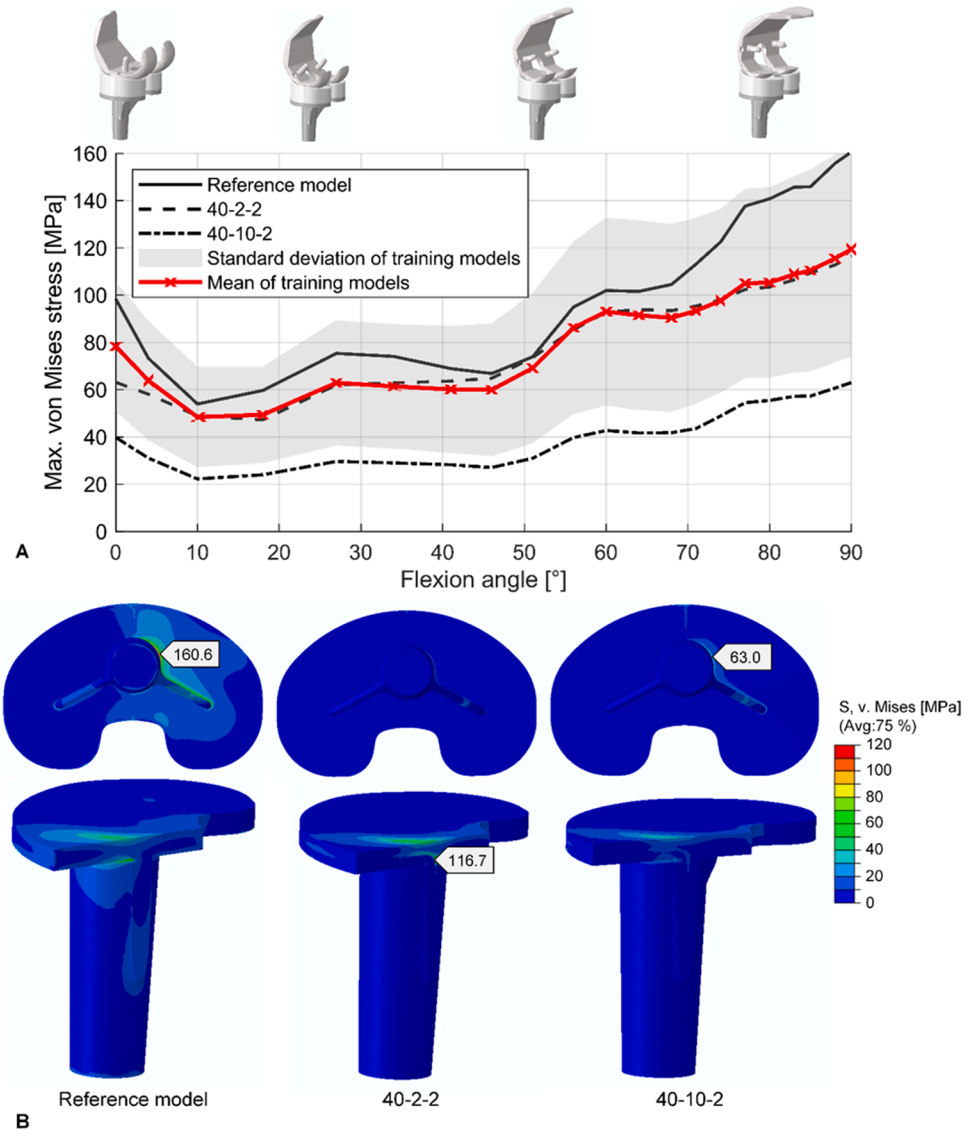

Fig. 6. Comparison of the reference model made of Ti-6Al-4V without an open porous surface and Pareto optimal parameter combinations of the Young`s modulus of the tibial tray (both 40 GPa), Young`s modulus of the open porous surface (2 or 10 GPa) and the thickness of the open porous surface (both 2mm). A) Maximum von Mises stress in the tibial tray in dependence on the flexion angle during the squat motion showing the mean and standard deviation of all training models as well as the Pareto optimal models and the reference model and B) von Mises stress field of the tibial tray (downside of the try and cut view) and indication of the maximum stress location at 90° knee flexion.

the respective titanium alloys and the mechanical performance of the open porous structures. The fatigue limit of titanium alloys is influenced by several factors, including their specific elemental composition and resultant microstructure [28,45,46], where the latter is affected by manufacturing methods and post-processing treatments such as aging. Unfortunately, fatigue limit data for materials that precisely match the defined parameter space were unavailable.

For reference, the fatigue limit of Ti-6Al-4V at a stress ratio (R) of 0.1 ranges between approximately 400 and 600 MPa [46]. Additionally, maximum cyclic stress values between 600 and 800 MPa have been reported in the literature [45]. Accordingly, the reference Ti-6Al-4V tibial tray, which exhibited a stress range of 144.2 MPa and a maximum stress of 160.6 MPa in this study, is expected to endure an effectively infinite number of cycles without fatigue failure (i.e., $>10^7$ cycles) under the applied loading conditions. Biomedical beta-titanium alloys have also demonstrated high fatigue strength under cyclic loading, with reported maximum cyclic stresses of 700 MPa for Ti-29Nb-13Ta-4.6Zr (Young's modulus: 74 GPa [28]), and 275 MPa for Ti-42Nb (Young's modulus: 60.4 GPa [42]). For alloys with stiffness levels closer to the Pareto-optimal parameters, such as Ti-19Nb-0.6O (Young's modulus: 42 GPa [27]), Ti-20Nb-6Ta (Young's modulus: 43.1 GPa [24]) or Ti-24Nb-4Zr-8Sn (Young`s modulus: 42 GPa [40]), no corresponding fatigue limit data could be identified in the literature.

However, based on the significantly lower stress levels observed in the Pareto-optimal configuration (stress range: 111.0 MPa; maximum stress: 116.7 MPa), it is reasonable to assume that a tibial tray composed of a beta-titanium alloy with a Young's modulus of 40 GPa and featuring an open porous surface (Young's modulus: 2 GPa; thickness: 2 mm) would also withstand the applied squat loading over a high number of cycles without fatigue failure.

In the Pareto-optimal tibial tray configuration with an open porous surface stiffness of 10 GPa, the peak stress (stress range: 54.0 MPa; maximum stress: 62.0 MPa) was localized within the porous surface structure. Consequently, the fatigue behavior of such additively manufactured porous architectures must be carefully considered. The mechanical performance of open porous structures, particularly stiffness and fatigue strength, is strongly influenced by porosity and cell geometry [24,38–40].

In this regard, Liu et al. [40] demonstrated that increased porosity significantly reduces fatigue strength, reporting cyclic maximum stresses below 10 MPa for open porous specimens fabricated from Ti-6Al-4V and Ti-24Nb-4Zr-8Sn. In contrast, Wu et al. [39] showed that with optimized cellular geometry, fatigue performance can be substantially improved. In their study, a topology-optimized Ti-25Nb-3Zr-3-Mo-1Sn structure with a Young's modulus of 2.2 GPa and a yield strength of 172 MPa achieved a fatigue strength of 46 MPa. More recently, Sass et al. [24] investigated Ti-20Nb-6Ta porous structures with a Young's modulus of 8.7 GPa and a yield strength of 179.2 MPa, further underlining the influence of alloy selection and microstructural control on mechanical performance.

Although design strategies such as geometry optimization can increase the fatigue resistance of open porous materials [39], avoiding high stress concentrations within the porous region remains desirable. Based on currently available literature data, the Pareto-optimal configuration 40-10-2, featuring an open porous surface Young's modulus of 10 GPa, seems incapable of withstanding the applied squat loading conditions over an extended number of cycles without fatigue failure.

This computational study is subject to the following limitations. The computational workflow is restricted by model assumptions that were previously reported [53,55]. Within this study, we have only used one patient-specific case in terms of bone properties and loading sequence, therefore, we did not consider anatomical variability. Thus, confirmation of the observations by different activities and a broader range of patients is needed for clinical translation of the results. The von Mises stresses observed in the tibial tray under severe loading conditions were evaluated in relation to reported fatigue limits of biomedical beta-titanium alloys. However, the complex interdependencies between elemental composition, microstructure, and the resulting mechanical properties, including both static and fatigue strength, present significant challenges for a comprehensive assessment. The open porous surface of the tibial tray was not geometrically modeled but assumed to be homogeneous with linear-elastic properties. Accurate FE simulation of open porous structures with sub-millimeter struts and plasticity requires complex model approaches. As a result, the stress in this layer is likely underestimated due to the reduced load-bearing cross-section and might be plastically deformed under more realistic model assumptions. Future studies should focus on optimizing the design of such structures for elasticity and fatigue endurance. Our results provide reasonable boundary conditions for guiding such studies. Furthermore, this study does not include experimental validation, which remains challenging due to limited access to human donor tissue and the complexity of replicating physiological conditions. Although literature based validation was conducted in this study and is commonly accepted in computational research [73], it is inherently constrained by variations in patient-specific bone geometry and loading conditions. Given these limitations, the current work relies on established modeling assumptions and focuses on a systematic comparison of material and design parameters. Future studies should include experimental data to further validate and refine the model predictions.

Given the outlined limitations, the findings of this study should be regarded as basis for identifying suitable ranges of material properties for beta-titanium alloys. Moreover, the work established a methodological framework that can be applied and refined in future investigations. Future research can expand on these results to guide the development of specific alloy compositions and structurally optimized designs that improve mechanical performance and long term fatigue resistance in cementless tibial tray applications. In particular, studies should incorporate fatigue life assessments of the investigated trays, using established fatigue theories [74,75].

Conclusion

This study systematically evaluated the mechanical performance of cementless tibial trays composed of beta-titanium alloys using a musculoskeletal multibody finite element model. By integrating a realistic patient-specific squat motion and simulating a wide range of material and design parameters, the analysis identified Pareto-optimal configurations that effectively minimize both periprosthetic stress shielding and stress concentrations within the implant. The results suggest that a tibial tray with a Young's modulus of 40 GPa and an open porous surface layer with a modulus between 2 and 10 GPa and a thickness of 2 mm offers the most promising balance of mechanical performance. These properties align with those of low-modulus beta-titanium alloys such as Ti/Nb/Ta, Ti/Nb/O, or Ti/Nb/Zr/Sn. The presented results define a feasible parameter space for future development and optimization of beta-titanium tibial trays.

Declaration of generative AI and AI-assisted technologies in the writing process

During the preparation of this work, the author(s) used Grammarly and DeepL Write to enhance the legibility of the manuscript and correct grammatical errors. After using this tool/service, the author(s) reviewed and edited the content as needed and take(s) full responsibility for the content of the published article.

Data availability

The data of this study are available upon reasonable request.

Funding

This work was supported by the German Federal Ministry of Education and Research (grant number: 03XP0279D), which had no role in study design; in the collection, analysis, and interpretation of data; in the writing of the report; and in the decision to submit the article for publication.

CRediT authorship contribution statement

Jan-Oliver Sass: Writing – review & editing, Writing – original draft, Visualization, Supervision, Project administration, Methodology, Investigation, Formal analysis, Data curation, Conceptualization. **Jonas Wenschuh:** Writing – review & editing, Methodology. **Florence Kosche:** Writing – review & editing, Methodology. **Rainer Bader:** Writing – review & editing, Supervision, Funding acquisition, Conceptualization. **Maeruan Kebbach:** Writing – review & editing, Visualization, Supervision, Project administration, Methodology, Investigation, Formal analysis, Data curation, Conceptualization.

Declaration of competing interest

The authors declare that they have no known competing financial interests or personal relationships that could have appeared to influence the work reported in this paper.

Appendix

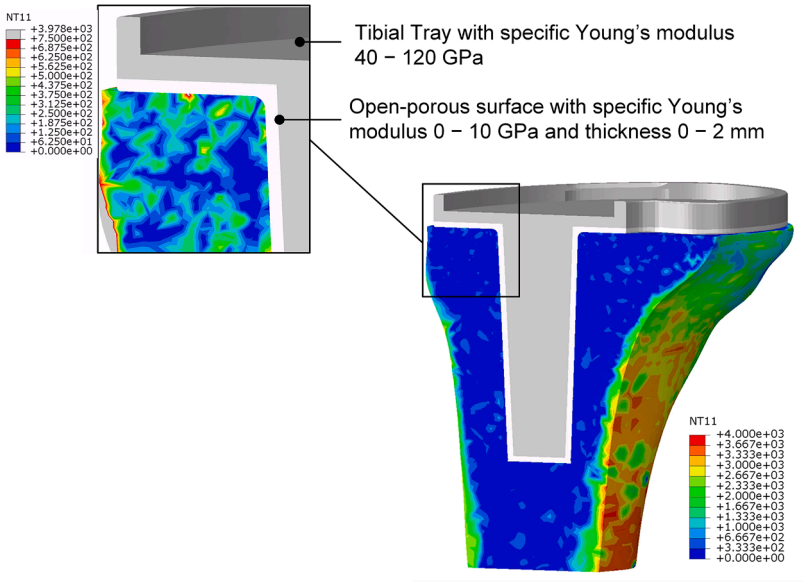

Fig. A1. Cut view of the tibial bone and tibial tray to illustrate the assigned material properties. The bone was modeled as heterogeneous by assigning Hounsfield units (HU) of the CT scan as virtual temperature values (Abaqus parameter NT11) and further assuming a temperature-dependent (HU-dependent) Young's modulus using a density-modulus relationship. The tibial tray was either modeled as completely dense or with an open-porous surface (here represented with a thickness of 1 mm) at the bone-implant interface.

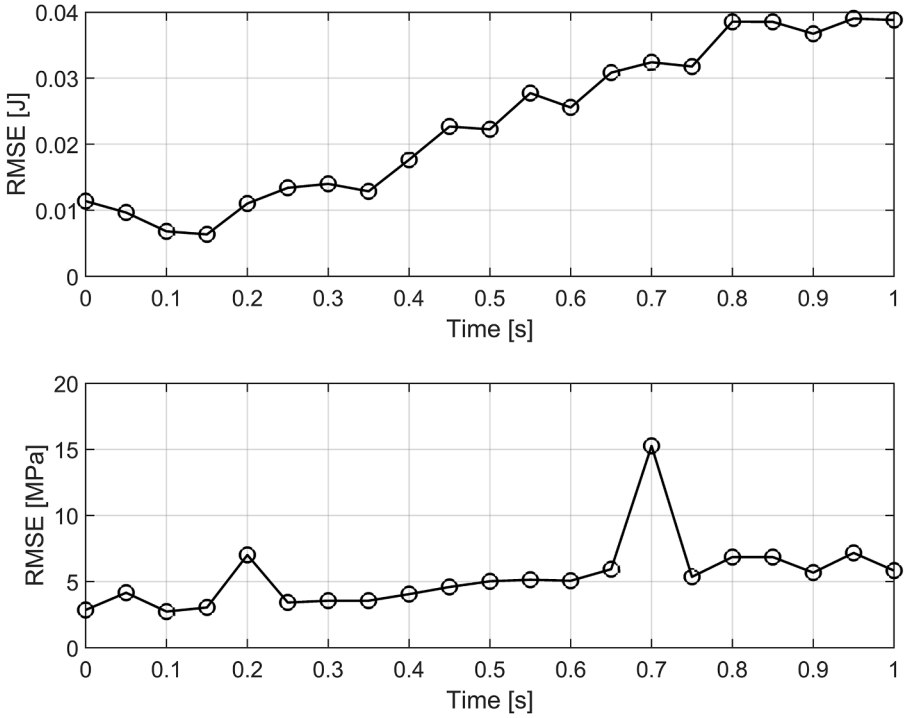

Fig. A2. Root mean square error (RMSE) of the 5-fold cross-validated trained Gaussian Process Regression models used to predict the A) strain energy in the bone ROI defined in the proximal tibia and B) maximum von Mises stress in the tibial tray under severed loading caused by a medial bone defect of the tibia plateau.

Table A1
Overview of the defined variables for the sensitivity analyses (YM_T: Young's modulus of the tibial tray material, YM_S: Young's modulus of the open-porous surface, S_T: thickness of the open porous surface). Twenty models were randomly selected based on the defined ranges and increments (YM_T: 40 to 120 GPa in 20 GPa increments, YM_S: 2 to 10 GPa in 2 GPa increments, S_T: 0 to 2 mm in 0.5 mm increments).

Model	YM_T [GPa]	YM_S [GPa]	S_T [mm]	Model	YM_T [GPa]	YM_S [GPa]	S_T [mm]
1	60	7	1	21	80	10	1

(continued on next page)

Table A1 (*continued*)

Model	YM_T [GPa]	YM_S [GPa]	S_T [mm]	Model	YM_T [GPa]	YM_S [GPa]	S_T [mm]
2	80	3	1.5	22	60	0	0
3	80	6	1	23	80	5	0.5
4	40	1	2	24	100	7	1
5	80	5	1.5	25	100	10	0.5
6	100	0	0	26	60	10	1.5
7	120	5	0.5	27	100	4	0.5
8	100	2	0.5	28	80	6	0.5
9	80	2	1.5	29	80	4	1.5
10	60	0	0	30	60	6	1
11	100	8	2	31	60	2	1
12	100	4	1.5	32	80	8	1
13	120	0	0	33	80	10	0.5
14	40	7	1.5	34	120	8	0.5
15	80	1	1.5	35	80	8	1.5
16	60	8	2	36	100	6	1
17	60	8	1	37	40	2	2
18	120	9	1	38	100	2	2
19	60	2	0.5	39	120	2	0.5
20	40	3	0.5	40	40	4	0.5

References

[1] J.T. Evans, R.W. Walker, J.P. Evans, A.W. Blom, A. Sayers, M.R. Whitehouse, How long does a knee replacement last? A systematic review and meta-analysis of case series and national registry reports with more than 15 years of follow-up, Lancet 393 (2019) 655–663, https://doi.org/10.1016/S0140-6736(18)32531-5.

[2] H. Inui, R. Yamagami, K. Kono, K. Kawaguchi, What are the causes of failure after total knee arthroplasty? J. Joint Surg. Res. 1 (2023) 32–40, https://doi.org/10.1016/j.jjoisr.2022.12.002.

[3] J.R.W. Crutsen, M.C. Koper, J. Jelsma, M. Heymans, I.C. Heyligers, B. Grimm, N.M. C. Mathijssen, M.G.M. Schotanus, Prosthetic hip-associated cobalt toxicity: a systematic review of case series and case reports, EFORT Open Rev. 7 (2022) 188–199, https://doi.org/10.1530/EOR-21-0098.

[4] A. Drynda, S. Drynda, J. Kekow, C.H. Lohmann, J. Bertrand, Differential effect of cobalt and chromium ions as well as CoCr particles on the expression of osteogenic markers and osteoblast function, Int. J. Mol. Sci. 19 (2018), https://doi.org/10.3390/ijms19103034.

[5] A. Jonitz-Heincke, M.-L. Sellin, A. Seyfarth, K. Peters, B. Mueller-Hilke, T. Fiedler, R. Bader, A. Klinder, Analysis of cellular activity short-term exposure to cobalt and chromium ions in mature human osteoblasts, Materials (Basel) 12 (2019), https://doi.org/10.3390/ma12172771.

[6] S. Yang, K. Zhang, F. Li, J. Jiang, T. Jia, S.-Y. Yang, Biological responses of preosteoblasts to particulate and ion forms of Co-Cr alloy, J. Biomed. Mater. Res. A 103 (2015) 3564–3571, https://doi.org/10.1002/jbm.a.35501.

[7] J.T. Munro, S. Pandit, C.G. Walker, M. Clatworthy, R.P. Pitto, Loss of tibial bone density in patients with rotating- or fixed-platform TKA, Clin. Orthop. Relat. Res. 468 (2010) 775–781, https://doi.org/10.1007/s11999-009-0794-x.

[8] B. Innocenti, E. Truyens, L. Labey, P. Wong, J. Victor, J. Bellemans, Can medio-lateral baseplate position and load sharing induce asymptomatic local bone resorption of the proximal tibia? A finite element study, J. Orthop. Surg. Res. 4 (2009) 26, https://doi.org/10.1186/1749–799X–4–26.

[9] G. Garabano, J. Rodriguez, L. Perez Alamino, C.A. Pesciallo, H. Del Sel, F. Lopreite, Stress shielding in total knee replacements: comparative analysis between titanium and all-polyethylene bases at 10 years follow-up, J. Orthop. 34 (2022) 276–281, https://doi.org/10.1016/j.jor.2022.09.007.

[10] J.-O. Sass, M. Kebbach, C. Lork, J. Johannsen, M. Weinmann, M. Stenzel, R. Bader, Computational biomechanical study on hybrid implant materials for the femoral component of total knee replacements, J. Mech. Behav. Biomed. Mater. 158 (2024) 106681, https://doi.org/10.1016/j.jmbbm.2024.106681.

[11] M. Fosco, R. Ben, L. Amendola, D. Dallari, D. Tigani, Management of bone loss in primary and revision knee replacement surgery, in: S. Fokter (Ed.), Recent Advances in Arthroplasty, InTech, 2012.

[12] A. Galas, L. Banci, B. Innocenti, The effects of different femoral component materials on bone and implant response in total knee arthroplasty: a finite element analysis, Materials (Basel) 16 (2023), https://doi.org/10.3390/ma16165605.

[13] K.S. Kang, T.N. Tien, M.C. Lee, K.-Y. Lee, B. Kim, D. Lim, Suitability of metal block augmentation for large uncontained bone defect in revision total knee arthroplasty (TKA), J. Clin. Med. 8 (2019), https://doi.org/10.3390/jcm8030384.

[14] Y. Liu, B. Chen, C. Wang, H. Chen, A. Zhang, W. Yin, N. Wu, Q. Han, J. Wang, Design of porous metal block augmentation to treat tibial bone defects in total knee arthroplasty based on topology optimization, Front. Bioeng. Biotechnol. 9 (2021) 765438, https://doi.org/10.3389/fbioe.2021.765438.

[15] F04 Committee, Practice for Cyclic Fatigue Testing of Metal Tibial Tray Components of Total Knee Joint Replacements, ASTM International, West Conshohocken, PA.

[16] International Organization for Standardization, Implants for Surgery — Total Knee-Joint Prostheses — Part 1: Determination of Endurance Properties of Knee Tibial Trays, 14879-1, ISO, 2020.

[17] J.J. Callaghan, D.E. DeMik, N.A. Bedard, A.N. Odland, W.M. Kane, S.M. Kurtz, Tibial tray fracture in a modern prosthesis with retrieval analysis, Arthroplast. Today 4 (2018) 143–147, https://doi.org/10.1016/j.artd.2017.12.005.

[18] A.D. Lam, G.P. Duffy, Early tibial component fractures in a cementless, 3d-printed, titanium implant, Arthroplast. Today 18 (2022) 31–38, https://doi.org/10.1016/j.artd.2022.08.002.

[19] M. Niinomi, Mechanical properties of biomedical titanium alloys, Mater. Sci. Eng. 243 (1998) 231–236, https://doi.org/10.1016/S0921-5093(97)00806-X.

[20] J.Y. Rho, M.C. Hobatho, R.B. Ashman, Relations of mechanical properties to density and CT numbers in human bone, Med. Eng. Phys. 17 (1995) 347–355, https://doi.org/10.1016/1350-4533(95)97314-f.

[21] E.F. Morgan, H.H. Bayraktar, T.M. Keaveny, Trabecular bone modulus-density relationships depend on anatomic site, J. Biomech. 36 (2003) 897–904, https://doi.org/10.1016/s0021-9290(03)00071-x.

[22] V. Apostolopoulos, P. Boháč, P. Marcián, L. Nachtnebl, M. Mahdal, L. Pazourek, T. Tomáš, Biomechanical comparison of all-polyethylene total knee replacement and its metal-backed equivalent on periprosthetic tibia using the finite element method, J. Orthop. Surg. Res. 19 (2024) 153, https://doi.org/10.1186/s13018–024–04631–0.

[23] G. Zhao, J. Luo, J. Ma, J. Wang, Decreased stress shielding with poly-ether-ether-ketone tibial implant for total knee arthroplasty - a preliminary study using finite element analysis, Heliyon 10 (2024) e27204, https://doi.org/10.1016/j.heliyon.2024.e27204.

[24] J.-O. Sass, M.-L. Sellin, E. Kauertz, J. Johannsen, M. Weinmann, M. Stenzel, M. Frank, D. Vogel, R. Bader, A. Jonitz-Heincke, Advanced Ti-Nb-Ta alloys for bone implants with improved functionality, J. Funct. Biomater. 15 (2024), https://doi.org/10.3390/jfb15020046.

[25] S. Ozan, J. Lin, Y. Li, R. Ipek, C. Wen, Development of Ti-Nb-Zr alloys with high elastic admissible strain for temporary orthopedic devices, Acta Biomater. 20 (2015) 176–187, https://doi.org/10.1016/j.actbio.2015.03.023.

[26] Y.L. Hao, S.J. Li, S.Y. Sun, C.Y. Zheng, Q.M. Hu, R. Yang, Super-elastic titanium alloy with unstable plastic deformation, Appl. Phys. Lett. 87 (2005) 091906, https://doi.org/10.1063/1.2037192.

[27] Y. Gao, J. Chen, Y. Gan, X. Liang, H. Chen, Da Zeng, C. Yang, W. Jiang, C. Ma, W. Xiao, Biomedical Ti–Nb–O alloy with high strength and ultra-low Young's modulus, Mater. Res. Lett. 13 (2025) 179–187, https://doi.org/10.1080/21663831.2024.2437402.

[28] S. Lei, J. Zhang, X. An, Y. Guo, X. Xu, Z. Ma, W. Yao, Q. Kong, Mechanical and corrosion properties of Ti–29Nb–13Ta-4.6Zr alloy prepared by cryomilling and spark plasma sintering, Vacuum 215 (2023) 112316, https://doi.org/10.1016/j.vacuum.2023.112316.

[29] R. Soni, S. Pande, S. Salunkhe, H. Natu, E. Abouel Nasr, R. Shanmugam, H.M.A. M. Hussein, In vitro and electrochemical characterization of laser-cladded Ti-Nb-Ta alloy for biomedical applications, Crystals 12 (2022) 954, https://doi.org/10.3390/cryst12070954.

[30] E. Eisenbarth, D. Velten, M. Müller, R. Thull, J. Breme, Biocompatibility of beta-stabilizing elements of titanium alloys, Biomaterials 25 (2004) 5705–5713, https://doi.org/10.1016/j.biomaterials.2004.01.021.

[31] Z. Guoqing, L. Junxin, Z. Chengguang, X. Juanjuan, Z. Xiaoyu, W. Anmin, Design optimization and manufacturing of bio-fixed tibial implants using 3D printing technology, J. Mech. Behav. Biomed. Mater. 117 (2021) 104415, https://doi.org/10.1016/j.jmbbm.2021.104415.

[32] N. Kladovasilakis, T. Bountourelis, K. Tsongas, D. Tzetzis, Computational investigation of a tibial implant using topology optimization and finite element

analysis, Technologies 11 (2023) 58, https://doi.org/10.3390/technologies11020058.
[33] Y. Li, Y. Ding, K. Munir, J. Lin, M. Brandt, A. Atrens, Y. Xiao, J.R. Kanwar, C. Wen, Novel β-Ti35Zr28Nb alloy scaffolds manufactured using selective laser melting for bone implant applications, Acta Biomater. 87 (2019) 273–284, https://doi.org/10.1016/j.actbio.2019.01.051.
[34] J.-O. Sass, J. Hembus, E. Fuhrmann, D. Vogel, E. Bauer, H.D. Link, R. Bader, Pre-clinical characterization of a novel flexible surface stem design for total knee replacements, Proc. Inst. Mech. Eng. H 237 (2023) 1154–1166, https://doi.org/10.1177/09544119231197596.
[35] J. Deering, K. Grandfield, Current interpretations on the in vivo response of bone to additively manufactured metallic porous scaffolds: a review, Biomater. Biosyst. 2 (2021) 100013, https://doi.org/10.1016/j.bbiosy.2021.100013.
[36] F. Günther, S. Pilz, F. Hirsch, M. Wagner, M. Kästner, A. Gebert, M. Zimmermann, Shape optimization of additively manufactured lattices based on triply periodic minimal surfaces, Addit. Manuf. 73 (2023) 103659, https://doi.org/10.1016/j.addma.2023.103659.
[37] Y. Liu, S. Cui, C. He, J. Li, Q. Wang, High cycle fatigue behavior of implant Ti-6Al-4V in air and simulated body fluid, Biomed. Mater. Eng. 24 (2014) 263–269, https://doi.org/10.3233/BME-130807.
[38] Y. Guo, C. Chen, L. Tan, Q. Wang, Y. Pan, H. Zhu, K. Zhou, C. Wu, The role of pore structures on the fatigue properties of additively manufactured porous tantalum scaffolds produced by electron beam powder bed fusion, J. Mater. Res. Technol. 19 (2022) 3461–3473, https://doi.org/10.1016/j.jmrt.2022.06.096.
[39] Z.Y. Wu, Y.J. Liu, X. Wu, X.C. Liu, J.C. Wang, Q. Wang, Fatigue performance of beta titanium alloy topological porous structures fabricated by laser powder bed fusion, J. Mater. Res. Technol. 29 (2024) 4772–4780, https://doi.org/10.1016/j.jmrt.2024.02.190.
[40] Y.J. Liu, H.L. Wang, S.J. Li, S.G. Wang, W.J. Wang, W.T. Hou, Y.L. Hao, R. Yang, L. C. Zhang, Compressive and fatigue behavior of beta-type titanium porous structures fabricated by electron beam melting, Acta Mater. 126 (2017) 58–66, https://doi.org/10.1016/j.actamat.2016.12.052.
[41] A.R. Hayyawi, H. Al-Ethari, A.H. Haleem, Development of β-Ti alloys for biomedical applications – a review, in: 2022 13th International Conference on Mechanical and Aerospace Engineering (ICMAE), IEEE, Bratislava, Slovakia, 2022, pp. 1–6.
[42] F. Günther, S. Pilz, L. Stampa, J. Bretschneider, M. Wagner, A. Gebert, M. Zimmermann, Defect-dependent fatigue properties of β Ti-42Nb processed by laser powder bed fusion, Mater. Today Commun. 43 (2025) 111733, https://doi.org/10.1016/j.mtcomm.2025.111733.
[43] Y.N. Hu, S.C. Wu, Z.K. Wu, X.L. Zhong, S. Ahmed, S. Karabal, X.H. Xiao, H. O. Zhang, P.J. Withers, A new approach to correlate the defect population with the fatigue life of selective laser melted Ti-6Al-4V alloy, Int. J. Fatigue 136 (2020) 105584, https://doi.org/10.1016/j.ijfatigue.2020.105584.
[44] A. Reck, S. Pilz, M. Calin, A. Gebert, M. Zimmermann, Fatigue properties of a new generation ß-type Ti-Nb alloy for osteosynthesis with an industrial standard surface condition, Int. J. Fatigue 103 (2017) 147–156, https://doi.org/10.1016/j.ijfatigue.2017.05.024.
[45] M. Niinomi, Fatigue performance and cyto-toxicity of low rigidity titanium alloy, Ti-29Nb-13Ta-4.6Zr, Biomaterials 24 (2003) 2673–2683, https://doi.org/10.1016/S0142-9612(03)00069-3.
[46] H.E. Boyer, Atlas of Fatigue Curves, Asm Intl.
[47] A.G. Au, V. James Raso, A.B. Liggins, A. Amirfazli, Contribution of loading conditions and material properties to stress shielding near the tibial component of total knee replacements, J. Biomech. 40 (2007) 1410–1416, https://doi.org/10.1016/j.jbiomech.2006.05.020.
[48] H. Bougherara, R. Zdero, Z. Mahboob, A. Dubov, S. Shah, E.H. Schemitsch, The biomechanics of a validated finite element model of stress shielding in a novel hybrid total knee replacement, Proc. Inst. Mech. Eng. H 224 (2010) 1209–1219, https://doi.org/10.1243/09544119JEIM691.
[49] Q.-H. Zhang, A. Cossey, J. Tong, Stress shielding in periprosthetic bone following a total knee replacement: effects of implant material, design and alignment, Med. Eng. Phys. 38 (2016) 1481–1488, https://doi.org/10.1016/j.medengphy.2016.09.018.
[50] H.-P.W. van Jonbergen, B. Innocenti, G.L. Gervasi, L. Labey, N. Verdonschot, Differences in the stress distribution in the distal femur between patellofemoral joint replacement and total knee replacement: a finite element study, J. Orthop. Surg. Res. 7 (2012) 28, https://doi.org/10.1186/1749-799X-7-28.
[51] L. de Ruiter, D. Janssen, A. Briscoe, N. Verdonschot, The mechanical response of a polyetheretherketone femoral knee implant under a deep squatting loading condition, Proc. Inst. Mech. Eng. H 231 (2017) 1204–1212, https://doi.org/10.1177/0954411917738805.
[52] D. Kluess, R. Souffrant, W. Mittelmeier, A. Wree, K.-P. Schmitz, R. Bader, A convenient approach for finite-element-analyses of orthopaedic implants in bone contact: modeling and experimental validation, Comput. Methods Programs Biomed. 95 (2009) 23–30, https://doi.org/10.1016/j.cmpb.2009.01.004.
[53] J.-O. Sass, K. Johnson, J.-B. Darques, L. Buerstenbinder, I. Soodmand, R. Bader, M. Kebbach, Influence of posterior cruciate ligament tension on tibiofemoral and patellofemoral joint contact mechanics in cruciate-retaining total knee replacement: a combined musculoskeletal multibody and finite-element simulation, Comput. Methods Biomech. Biomed. Engin. (2024) 1–13, https://doi.org/10.1080/10255842.2024.2329946.
[54] B.J. Fregly, T.F. Besier, D.G. Lloyd, S.L. Delp, S.A. Banks, M.G. Pandy, D.D. D'Lima, Grand challenge competition to predict in vivo knee loads, J. Orthop. Res. 30 (2012) 503–513, https://doi.org/10.1002/jor.22023.
[55] M. Kebbach, M. Darowski, S. Krueger, C. Schilling, T.M. Grupp, R. Bader, A. Geier, Musculoskeletal Multibody Simulation Analysis on the Impact of Patellar Component Design and Positioning on Joint Dynamics after Unconstrained Total Knee Arthroplasty, Materials (Basel) 13 (2020), https://doi.org/10.3390/ma13102365.
[56] M. Kebbach, A. Geier, M. Darowski, S. Krueger, C. Schilling, T.M. Grupp, R. Bader, Computer-based analysis of different component positions and insert thicknesses on tibio-femoral and patello-femoral joint dynamics after cruciate-retaining total knee replacement, Knee 40 (2023) 152–165, https://doi.org/10.1016/j.knee.2022.11.010.
[57] T. Tischer, A. Geier, C. Lutter, A. Enz, R. Bader, M. Kebbach, Patella height influences patellofemoral contact and kinematics following cruciate-retaining total knee replacement, J. Orthop. Res. 41 (2023) 793–802, https://doi.org/10.1002/jor.25425.
[58] B. Helgason, F. Taddei, H. Pálsson, E. Schileo, L. Cristofolini, M. Viceconti, S. Brynjólfsson, A modified method for assigning material properties to FE models of bones, Med. Eng. Phys. 30 (2008) 444–453, https://doi.org/10.1016/j.medengphy.2007.05.006.
[59] F. Taddei, A. Pancanti, M. Viceconti, An improved method for the automatic mapping of computed tomography numbers onto finite element models, Med. Eng. Phys. 26 (2004) 61–69, https://doi.org/10.1016/S1350-4533(03)00138-3.
[60] D. Vogel, M. Klimek, M. Saemann, R. Bader, Influence of the acetabular cup material on the shell deformation and strain distribution in the adjacent bone-a finite element analysis, Materials (Basel) (2020) 13, https://doi.org/10.3390/ma13061372.
[61] J.P. Halloran, A.J. Petrella, P.J. Rullkoetter, Explicit finite element modeling of total knee replacement mechanics, J. Biomech. 38 (2005) 323–331, https://doi.org/10.1016/j.jbiomech.2004.02.046.
[62] M. Woiczinski, C. Tollrian, C. Schröder, A. Steinbrück, P.E. Müller, V. Jansson, Calculation of the elastic properties of prosthetic knee components with an iterative finite element-based modal analysis: quantitative comparison of different measuring techniques, Biomed. Tech. (Berl) 58 (2013) 369–376, https://doi.org/10.1515/bmt-2013-0003.
[63] O. Roffmann, M. Stiesch, A. Greuling, Preventing stress singularities in peri-implant bone - a finite element analysis using a graded bone model, Comput. Methods Biomech. Biomed. Engin. 27 (2024) 547–557, https://doi.org/10.1080/10255842.2023.2190832.
[64] N. Armillotta, E. Bori, B. Innocenti, Finite element analysis of malposition in bi-unicompartmental knee arthroplasty, Arch. Orthop. Trauma Surg. 143 (2023) 3447–3455, https://doi.org/10.1007/s00402–022–04656–2.
[65] C.E. Rasmussen, Gaussian processes in machine learning, in: O. Bousquet, U. von Luxburg, G. Rätsch (Eds.), Advanced Lectures on Machine Learning, Springer Berlin Heidelberg, Berlin, Heidelberg, 2004, pp. 63–71.
[66] K. Dammak, A. El Hami, Multi-objective reliability based design optimization using Kriging surrogate model for cementless hip prosthesis, Comput. Methods Biomech. Biomed. Eng. 23 (2020) 854–867, https://doi.org/10.1080/10255842.2020.1768247.
[67] Y.-C. Cheng, C.-P. Jiang, D.-H. Lin, Finite element based optimization design for a one-piece zirconia ceramic dental implant under dynamic loading and fatigue life validation, Struct. Multidisc. Optim. 59 (2019) 835–849, https://doi.org/10.1007/s00158-018-2104-2.
[68] D. Yudistiro, Y.-C. Cheng, Optimization and innovative design of dental implants under dynamic finite element analysis, J. Chin. Inst. Eng. 46 (2023) 615–627, https://doi.org/10.1080/02533839.2023.2227878.
[69] S. Barati, N. Fatouraee, M. Nabaei, L. Petrini, F. Migliavacca, G. Luraghi, J.F. R. Matas, Patient-specific multi-scale design optimization of transcatheter aortic valve stents, Comput. Methods Programs Biomed. 221 (2022) 106912, https://doi.org/10.1016/j.cmpb.2022.106912.
[70] H.M. Frost, Bone's mechanostat: a 2003 update, Anat. Rec. A Discov. Mol. Cell. Evol. Biol. 275 (2003) 1081–1101, https://doi.org/10.1002/ar.a.10119.
[71] T.A. Enab, N.E. Bondok, Material selection in the design of the tibia tray component of cemented artificial knee using finite element method, Mater. Des. 44 (2013) 454–460, https://doi.org/10.1016/j.matdes.2012.08.017.
[72] N. Noraphaiphipaksa, R. Borrisutthekul, C. Kanchanomai, Effect of malaligned knee prosthesis on stress and fatigue life of tibial tray, Eng. Fail. Anal. 137 (2022) 106252, https://doi.org/10.1016/j.engfailanal.2022.106252.
[73] C. Oefner, S. Herrmann, M. Kebbach, H.-E. Lange, D. Kluess, M. Woiczinski, Reporting checklist for verification and validation of finite element analysis in orthopedic and trauma biomechanics, Med. Eng. Phys. 92 (2021) 25–32, https://doi.org/10.1016/j.medengphy.2021.03.011.
[74] A. Mehboob, I. Barsoum, H. Mehboob, R.K. Abu Al-Rub, A. Ouldyerou, 2024. Topology optimization and biomechanical evaluation of bone plates for tibial bone fractures considering bone healing. Virtual and physical prototyping 19, e2391475. https://doi.org/10.1080/17452759.2024.2391475.
[75] A. Mehboob, H. Mehboob, A. Ouldyerou, I. Barsoum, Computational biomechanical analysis of Ti-6Al-4V porous bone plates for lower limb fractures, Mater. Des. 240 (2024) 112842, https://doi.org/10.1016/j.matdes.2024.112842.